On the Coupling of the Low-Latitude Ionosphere under Solar Perturbation and Tropospheric Forcing

[1,2]Abhijit Banerjee, [1]Rina Bhattacharya
[1] Department of Physics, JIS University, Kolkata, India
[2]Department of Computer Science, New Alipore College, Kolkata, India

Corresponding Author: Abhijit Banerjee

Abstract: The ionospheric plasma responds concurrently to solar forcing and upward disturbances from the weather laden troposphere yet the relative contributions of each remains poorly quantified at low latitudes. This study bridges that gap by analysing the data sets covering pre-monsoon (March–May 2019-2020), monsoon (June–September 2019-2020) and a convective low-pressure phenomenon (July 2021) above the Tropical Gangetic Delta. This work integrates radiosonde thermodynamics (CAPE, precipitable water, relative humidity at 850 hPa, lapse rate) with hourly GPS and ionosonde TEC to compute a Moisture Coupling Index and perform principal-component analysis. Comparison between physics-informed synthetic TEC with observations reveals excellent skill except on storm days when complex dynamics depress the model estimates. Combination of wavelet-derived atmospheric-gravity-wave (AGW) spectra with ELF–VLF measurements are carried out to quantify the coupling strength via a significant scoring scheme. Long-period AGWs (~7.8 h) consistently amplify the TEC (> 90 %) while shorter high-power waves yield weaker effects by underscoring the primacy of resonance and propagation efficiency over amplitude. Schumann -resonance fundamentals and harmonics strengthened during the convective peaksconfirms an active Earth–ionosphere cavity. Overall solar control is minimal (TEC–F10.7: $r \approx 0.084$); the strongest negative relation is between CAPE and TEC ($r = -0.083$), whereas moisture variables show mixed polarity. July 2021 phenomenon demonstrates that intermediate-period AGWs can elevate TEC variability to ~ 77 % without extreme power, while a high-power 4 hrs. wave produces only 37 %, thus indicating a dissipation when frequencies are mismatched. Results reveal that seasonally driven tropospheric instabilities dominate low-latitude ionospheric variability whileanalyzed through a novel framework by integrating thermodynamic diagnostics, TEC modellingalong with AGW, ELF and VLF-based wave-resonance characterization.

Keywords: Radiosonde, CAPE, TEC, AGW, ELF-VLF, Schumann resonance, Spectrum

1. Introduction

The concentration of the ionic plasma within ionosphere modifies and restores according to the introduction and the removal solar perturbation effect in daily basis. It producesa specific pattern of total electron content: TEC, electron density of F_2 and total ionosphere (N_mF_2 and Ne) and the plasma frequency of F_2layer (f_oF_2) respectively[1,2]. The tropospheric effect like pre-monsoon and monsoonal instabilities and anonymous monsoon and mesoscale hybrid effects introduces anomalies in the usual diurnal electron content and thereby in the conductivity to these low latitude ionsopsheric parameters by introducing upward forcing [3]. The investigation of troposphere-ionosphere coupling mechanisms has evolved significantly since the revolutionary work of first theorization of the Earth-ionosphere cavity resonances carried out by Schumann (1952) [4]. Subsequent experimental verification by Balser and Wagner (1960) [5] established the foundation for understanding how the electromagnetic phenomena in the lower atmosphere could influence by ionospheric processes. Early theoretical frameworks developed by Rycroft etal. (2000) [6] described the global atmospheric electric circuit, identifying thunderstorms as principal generators of current systems that extend into the ionosphere. Williams (1992) [7] further clarified the relationship between global lightning activity and Schumann resonances, while the Spread FEx campaign provided crucial insights into the atmospheric gravity wave (AGW) propagation from tropospheric convection to ionospheric altitudes as shown by Fritts etal.(2009) [8]. More recent work by Abdu et al. (2021) [9] demonstrated the measurable enhancements in Schumann resonance amplitudes during monsoon low-pressure systems, suggesting intensified troposphere-ionosphere coupling during such events. Banerjee and Bhattacharya (2021) [10] have analysed pre-monsoon and monsoon thunderstorm events over the Gangetic West Bengal using 2019–2020 radiosonde data. Stability indices like KI, LI, SWI, CAPE, CIN and BRN revealed distinct seasonal instability patterns with stronger convective inhibition in pre-monsoon and organized convection in monsoon. Banerjee (2022) [11] studied a July 2021 low-pressure event by showing increased instability and heavy rainfall linked to cyclonic circulation. Radiosonde data revealed significant changes in humidity, wind, lapse rates and convective indices thus confirming the value of upper-air analysis for predicting localized severe weather in eastern India. Gong et al. (2019) [12] noted monsoon-specific modulations in ionospheric behaviour, but comparative studies between pre-monsoon and monsoon periods have lacked temporal depth and physical integration. Wilson et al. (2006) [13] highlighted the absence of real-time analyses during extreme convective events, while few studies[14] pointed out the need for a unified approach for integrating atmospheric gravity waves (AGWs), ELF-VLF signals and thermodynamic analyses. The present study investigates troposphere and ionosphere coupling across seasonal scales while aiming to address critical research gaps as identified. This study extends upon the foundational work of Banerjee & Bhattacharya

(2020)[10]; Banerjee (2022)[11] by introducing a structured methodology across three phases: (1)coupling analysis through TEC and thermodynamics modelling (monsoon and pre-monsoon) (2) same for the low pressure belt and (3) AGW and ELF-VLF spectral analysis. The timeframes analysed include pre-monsoon (March–May 2019–2020), monsoon (June–September 2019–2020) and a low-pressure belt event (July 2021) over the Tropical Gangetic Delta. Although the first phase incorporates the meteorological, solar flux and ionospheric data to assess instabilities but in second the low-pressure event is separately analysed with different visualization techniques. Thermodynamic indices such as CAPE (i.e.potential energy available for convection), relative humidity (RH) at 850 hPa, lapse rate (Γ) and precipitable water (PW) are calculated from radiosonde data alongside the solar flux (F10.7) and ionospheric (TEC) parameters. These inputs support the computation of a Moisture Coupling Index (MCI) and Principal Component Analysis (PCA) to understand coupling dynamics [15,16]. Values of modelled(physics informed synthesis) and observed TEC are compared. The final analytical phase characterizes AGW and ELF-VLF behaviour to determine coupling strength. Schumann resonances (fundamental and harmonics) identified in the ELF spectra, particularly during strong vertical coupling [17-20]. Coupling strength is further assessed by using an advanced scoring system. Hourly TEC data from ionosondes and GPS stations are reconstructed for data-sparse periods [21,22]. Results show a weak overall solar and TEC correlation ($r \approx 0.084$), emphasizing the limited role of solar influence during certain convective events. CAPE and TEC exhibit the strongest (negative) relationship (-0.083), suggesting that intense convective activity reduces the electron density. RH at 850 hPa shows positive TEC correlation, while PW exhibits a negative correlation thus indicating complex moisture-ionosphere interactions. During the low-pressure system intermediate-period AGWs generate the highest TEC variability (~77%). ELF peaks support strong troposphere-ionosphere interactions. However, high AGW or ELF power alone does not guarantee strong TEC responses, suggesting dissipation during propagation that limits the coupling efficiency. Overall, it can be said that not just amplitude the resonance characteristics and wave period determines the effective coupling. This study establishes that strong, seasonally dependent tropospheric instabilitiese specially during pre-monsoon and convective low-pressure systems that can modulate the ionosphere via AGW and ELF-VLF mechanisms, with moisture and thermodynamic conditions playing a critical role in this vertical coupling.

2. Methodology

Following are the methods of analytical approach to investigate the coupling mechanisms between the troposphere and ionosphere, combining physical reference-based modelling with statistical diagnostics. The choice of dates from 2019 and 2020 depends on their time of occurrence, predictions and ease of their instability and demarcated as perturbed day (PD) and unperturbed day (UD) during pre-monsoon

and monsoon season as given in the work of Banerjee and Bhattacharya (2020) [10]. These dates are as follows: May 20 and 21, 2019 (PD), June 23 and 24, 2019 (UD), September 12 and 13, 2019 (UD), December 15and 16, 2019 (UD), February 10 and 11, 2020 (UD), April 18 and 19, 2020 (PD) and August 24and 25, 2020 (PD).Although these days are considered by keeping in mind about the pre-monsoon and monsoon seasons but few days are considered here to mark the responses of the typical fair weather condition as they are falling in the month of February, December and January. Therefore, they are representing the winter season so the category named as "other season" has been introduced to cover all these dates in the analysis. Again the dates for the event of low pressure belt on the late of July, 2021 as mentioned in Banerjee (2022) [11] are as following: July 26, 2021 (Fair weather to initialisation of low pressure belt), July 27, 2021(Growth phase continuation), July 28, 2021 (Growth phase maximization), July 29, 2021(Strom day) and July 30, 2021 (Decay phase). The input data set of ionospheric TEC, N_mF_2, Ne and f_oF_2 are considered here with the atmospheric metadata.

Phase 1.TEC and thermodynamics modelling (monsoon and pre-monsoon):

Step 1. Data Modelling and Parameterization: The ionospheric parameters TEC, N_mF_2, Ne and $f_oF_2$are modelled using diurnal, seasonal and solar influences as they applied to pre-processed datasets. Here TEC, F10.7 solar flux with an 11-year solar cycle and diurnal variation are modelled [22,23,24].

$\mathbf{TEC(t) = TEC_{base} + A\sin(\frac{2\pi(t-\phi)}{24}) + \eta(t)}$; Where A = amplitude (season-dependent: Pre-Monsoon =5, Monsoon = 4, other = 6), $\boldsymbol{\phi}$ = phase shift (local noon = 12 UTC).

$\mathbf{F_{10.7} = 70 + 30\sin\left(\frac{2\pi(t-t_0)}{11\times365.25}\right) + \eta(t)}$; Where: $\mathbf{t_0}$=reference year (2019)

Here, $\boldsymbol{\eta(t)}\sim\mathbf{N(0,\sigma^2)}$ = Gaussian noise ($\boldsymbol{\sigma}$ = 1–2 TECU)

Tropospheric stability indices using the thermodynamic parameters [17,25,26] viz. CAPE, lapse rate and precipitable water are also modelled. The electron density profile $\mathbf{N_e(h)}$ follows the Chapman layer model [27].

$$\mathbf{N_e(h) = N_m exp\left[\frac{1}{2}\left(1 - \frac{h - h_m}{H} - exp\left(-\frac{h - h_m}{H}\right)\right)\right]}$$

With solar modulation [28]$\mathbf{S(t) = 0.8 + 0.2\sin(2\pi t/11)\ years}$

Diurnal effects [29]: $\mathbf{D(t) = 0.7 + 0.3\sin(\frac{2\pi(LT-6)}{24})}$

Geomagnetic influence [30]:$\mathbf{G(t) = 1 + 0.1K_p index}$

Step 2.PCA and MCI estimation: Correlation between TEC and tropospheric parameters $\mathbf{X = [TEC, CAPE, RH, \Gamma, F_{10.7}]}$ is computed via Pearson's correlation coefficient [31]: $\mathbf{r = \frac{Cov(TEC,X)}{\sigma_{TEC}\sigma_X}}$

Dimensionality reduction is performed by using Principal Component Analysis (PCA) with eigen-decomposition [32]. Eigen-decomposition: $\mathbf{X^TX = V\Lambda V^T}$ and the Moisture Coupling Index (MCI) defined as:$\mathbf{MCI} = \frac{\mathbf{RH_{850}PW}}{\mathbf{TEC+\epsilon}}$

Step 3. Model Validation Metrics: Following matrices are estimated in this work.

Root Mean Square Error (RMSE): $\mathbf{RMSE} = \sqrt{\frac{1}{N}\sum_{i=1}^{N}(\mathbf{TEC_{obs} - TEC_{model}})^2}$

Normalized Residuals: $\mathbf{Res_{norm}} = \frac{\mathbf{TEC_{obs} - TEC_{model}}}{\sigma_{TEC}}$

Autocorrelation Function (ACF):$\mathbf{ACF(\tau)} = \frac{\mathbf{E[(TEC(t)-\mu)(TEC(t+\tau)-\mu)]}}{\sigma^2}$

Phase 2.TEC and thermodynamics modelling (low-pressure belt)

The analyses of the meteorological and ionospheric responses during the low-pressure belt event in July 2021 are structured in a six-step framework.

Step 1. Construction of a temporal grid over a 24-hour diurnal cycle with 500 equidistant time points to represent local time dynamics.

Step 2. The primary external driversas solar flux and geomagnetic activityare modelled with sinusoidal components peaking at noon and dusk respectively with incorporating Gaussian noise to simulate natural variability.

Step 3. Focuses on tropospheric variablesviz. CAPE shows an afternoon maximum while PW and RH peaks at near noon, modulated further by growth, storm and decay phases of the low-pressure event.

Step4. The ionospheric response is represented by the TEC simulated separately for each phase. The growth phase shows early morning TEC maxima influenced by solar flux and moisture coupling. The storm day depicts reduced TEC baseline and enhanced 6-hour oscillations with the strongest negative moisture-ionosphere correlation. The decay phase is characterized by an elevated TEC baseline and 8-hour modulation. The moisture-ionosphere coupling strength is captured via time-dependent coupling indices κ(t)that vary with phase.

Step 5.Introduces physical constraints, setting permissible ranges for TEC (5–30 TECU), CAPE (500–2000 J/kg), RH (30–90%) and κ (0.5–1.0), along with noise margins.

Step 6.Validates the models using residual analysis and correlation checks thereby ensuring physical likelihood with TEC residuals within 0.4–0.6 TECU and solar or geomagnetic influences kept minimal**.**

These stated approaches are captured by the following representative equations across the phases of the low pressure belt.[Gaussian Noise: N(μ,σ); μ =mean & σ =standard deviation]

Step 1. Temporal frame work:$t_i = \frac{24i}{N}$; for i=0,...,N-1 (N=500)

Step 2. Solar Flux:$S_i = 100 + 20\sin\left(\frac{2\pi(t_i-12)}{24}\right) + \eta_S$; $\eta_S \sim N(0,5)$

Geomagnetic Activity: $G_i = 100 + 10\sin\left(\frac{2\pi(t_i-18)}{24}\right) + \eta_G$; $\eta_G \sim N(0,3)$

Step 3. Tropospheric variables are as estimated

Convective potential:$\mathrm{CAPE(t)} = 1000 + 300\sin\left(\frac{2\pi(\mathrm{t}-15)}{24}\right) + \mathrm{N}(0,50)$

Moisture parameters: $\mathrm{PW(t)} = 40 + 10\sin\left(\frac{2\pi(\mathrm{t}-12)}{24}\right) + \mathrm{N}(0,5)$

$$\mathrm{RH(t)} = \mathrm{A} + \mathrm{B}\sin\left(\frac{2\pi(\mathrm{t}-12)}{24}\right) + \mathrm{N}(0,\ \sigma_k{}^2)$$

For growth,storm and decay LPB (A, B, σ_k) = ((65, 75, 60), (15, 10, 10), (5, 5, 4))

Step 4. Phase-Specific Modelling:

$$\mathrm{TEC}(t) = A + B\,sin\left(\frac{2\pi(t-6)}{24}\right) + Cs(t) + N(0,\ \sigma_j)$$

$$TEC(t)_{Physics} = TEC(t)[1 + D\,sin\left(\frac{2\pi t}{12}\right)] + EG(t)$$

$$\kappa_{Growth}(t) = \kappa_i(t) + G\,sin\left(\frac{2\pi(t-9)}{24}\right) + N(0,\ \sigma_i)$$

Grouped by variable across the three phases (growth, storm, decay): A=(15,12,18),B=(5,4,6),C=(0.1,0.08,0.12), σ_j=(1,1.2,0.8),D=(0.5,0.59,0.745),E=(0.05,0.03,0.07),$\kappa_i(t)$=(0.8,0.85,0.7),G=(0.15,0.1,0.2) and σ_i=(0.05,0.04,0.06)

Phase 3.AGW and ELF-VLF spectral modelling: This workflow quantifies the troposphere–ionosphere coupling during pre-monsoon, monsoon and low-pressure-belt periods through the following six operations.

Step 1. Acquires hourly TEC and daily F10.7 data to fill sub-hourly gaps with a diurnalplusannual sinusoid and merges the two series within a ±1 hrs.window.

Step 2. Removes non-stationary trends (quadratic fit and fall-back to median at the necessity) [33], scales the residuals with Median Absolute Deviation (MAD) and isolates AGW signatures via complex-Morlet wavelet power at 2–8 hoursband retaining only those with Signal to Noise ratio (SNR) > 3and exceeding 95th-percentile threshold [34-36].

Step 3. Characterises ELF–VLF emissions through Welch-PSD(Power spectral density) [18] on 1024-point Hann segments with the generation of integrated ELF (3 Hz–3 kHz) and VLF (3–30 kHz) power and flags Schumann-resonance peaks at canonical frequencies [35-37].

Step 4. Converts these diagnostics into coupling metricsviz.TEC variability (percentage), AGW power, ELF–VLF energy, Schumann-peak countand scores each hour (0–6) to classify coupling as weak, moderate or strong [38,39].

Step 5. Synthesises of realistic signals by superposing seasonal TEC oscillations, AGW-modulated ELF–VLF sinusoids [40], anthropogenic carriers and lightning-pulse spherics [41] are carried out.

Step 6. Scales peak counts and injects spectrally-shaped noise to emulate seasonal variability. This pipeline links upper-atmospheric electrodynamics, lower-atmospheric

instability and geophysical wave propagation in a single and statistically validated framework.

Following are the mathematical details of modelling corresponds to the steps

Step 1. Gap-fill TEC:$\boldsymbol{y_{synthetic}(t) = 5\,sin\left(\frac{2\pi t}{24}\right) + 2\,sin\left(\frac{2\pi t}{8760}\right) + N(0, 1.5)}$

Step 2. Wavelet power (complex -Morlet: cmor1.5-1.0) shown by Periodogram:

$W(s,\tau) = \int_{-\infty}^{\infty} y_{norm}(t)\frac{1}{\sqrt{s}}\psi^*(\frac{t-\tau}{s})dt$;s$\epsilon${2,8}$hrs$

Step 3. Welch PSD:$P_k(f) = \frac{1}{MU}\left|\sum_{n=0}^{m-1} w(n)\, x_k(n)e^{-2\pi i f_n}\right|^2$

Window (Hann) function: $w(n)$, Where, $0 \le n \le m-1$,Normalization factor is U

Schumann Resonance: Peaks identified at frequencies f_s (Hz) [9, 38]

$f_S \in$ {7.83,14.3,20.8,26.4,33.2}and PSD(average): $\hat{P}(f_s) > 0.5 \times max\,(\hat{P}(f)\big|_{3Hz \le f \le 3kHz}$,

Step 4.TEC Variability= $\frac{\sigma_{TEC}}{\mu_{TEC}} \times 100\%$,$P_{AGW} = \sum_{Wavelet\ scale \in |S_{min}, S_{max}|} P(Wavelet\ scale, \tau)\ dB$: $10\,log_{10}(P_{AGW})$

Scoring System:$\boldsymbol{s = \sum_{i=1}^{6} I(C_i)}$;Where,$\sum_{i=1}^{6} \boldsymbol{C_i}$=$P_{AGW}$ > {15,20,10,15}dB and $N_{Schumaan} \ge$ {2,3} andclassified as Strong (≥4), Moderate (2–3), Weak (<2).

Step 5. Synthetic TEC: $TEC(t) = 20 + 10\,sin\frac{2\pi(t-6)}{24} + \Delta_{season} + \sum_{k=1}^{3} A_k\,sin\left(\frac{2\pi t}{T_k} + \emptyset_k\right) + \epsilon(t)$

Where, Δ_{season}modulates seasonal effects (pre-monsoon:5, monsoon: 3).

ELF-VLF emulation:

$$S(t) = \sum_{k=1}^{5} \alpha_k \sin 2\pi f_k \left(1 + \beta \sin \frac{2\pi t}{3600 T_{AGW}}\right) + \gamma TEC(t)\eta(t) + \sum_{j=1}^{3} \beta_i \sin 2\pi f_i t + \sum_{i} k_i e^{-\frac{(t-t_i)}{\tau}} \Pi_i(t)$$

Where, anthropogenic noise $\eta(t)\sim N(0,1)$ and lightning pulses$\Pi_i(t)$=Rectangular pulse,at t_i, τ =0.5ms (decay time)

Step 6. Seasonal variability Model

Peak count adjustment:$N_{Peaks} = \min(\left|N_{base}\left(0.5 + \frac{P}{10}\right)\right| \lambda_{season}, N_{max})$

Where,N_{base} (Monsoon: 4, Premonsoon: 2),λ_{season}(Monsoon: 1.5, Premonsoon: 1)

Noise injection:$\hat{P}_{modified}(f) = \hat{P}(f)[1 + 0.1p(0.8 + 0.4U)]$

Optimization and convergence: Here 10 consecutive passes or iteration from steps 1 to 6 of phase 3 are carried out with controlled variations of peak count adjustment factor and noise injection factor in parameters to simulate the variability in real-time manner thereby optimizing the detection thresholds for different seasons leading to the validation of the robustness of the method. The convergence from the iterations has occurred out of the results (AGW detection, Schumann peaks and coupling scores)

at the achievement of the stabilization at the progress with a consistent set of parameters that work across all the seasons.

Soft-ware tools and implementation: For executing this methodology we have used python (version: Python 3.11.13) programming plat form in Google Colab environment with T4-GPU runtime type activation.

3. Data sources

Atmospheric parameters are collected from the radiosonde data sources at upper weather section of Wyoming University for the station Calcutta/Dumdum and Dhaka (Bangladesh). The metadata curated from the results of Banerjee and Bhattacharya (2020) and Banerjee (2021) [10, 11].CCMC/NASA (Model-2020) of IRI 2020 for ionopsheric (ionosonade and GPS) parameters for Calcutta day based hourly data set of TEC, N_mF_2, Ne and f_0F_2 and forF10.7 data NOAA's Space Weather Prediction Center (SWPC) and NASA OMNI-Web (GSFC, SPDF) is accessed.

4. Results and Discussions

Phase 1.TEC and thermodynamics modelling (monsoon and pre-monsoon): The following are the results obtained from the coupling analysis of pre-monsoon (March-May 2019-2020) and monsoon (June-September 2019-2020) season.

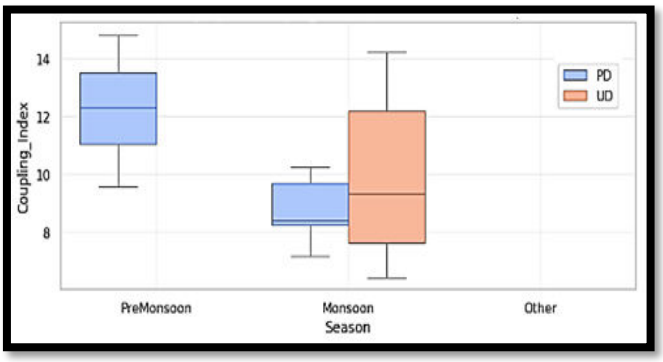

Fig.1 Box Plot for Tropospheric Coupling Indices (Coupling_Index) across pre-monsoon, monsoon and others seasons

Figure 1 shows that only pre-monsoon perturbed days exhibit consistently strong, stable coupling indices. It clusters tightly between 9.5 and 14.5 (median ≈ 12.5). Monsoon shows both PD and UD. PD values are narrower (7.0–10.5; median= 9), while UD spans 6.5–14.5 (median= 9.2), indicating convection-driven variability. The "other season" yield negligible indices hence implying weak coupling.

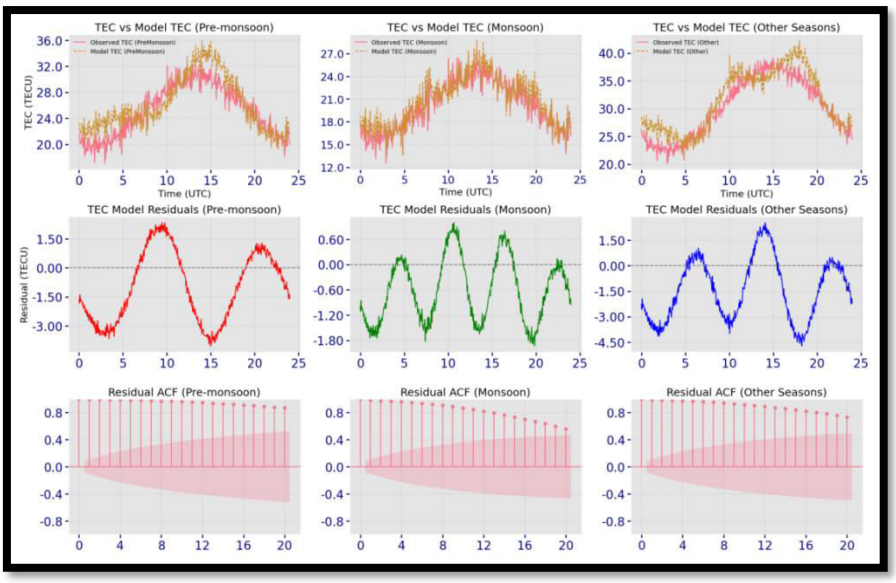

Fig.2 Comparison of observed and modelled TEC for pre-monsoon (left), monsoon (middle) and other seasons (right). Top panels show diurnal observed and model TEC variations in amplitude and phase for three seasonal. Middle panels display residuals (Observed & Model) (along ordinate) all three seasons. Bottom panels present autocorrelation functions (ACF) (along ordinate) of the residuals for all the seasons with temporal dependence (Abscissae in UT).

Figure 2 shows observed TEC peaks at 13–15 UTC in every regime but the amplitudes differs as: 20–34 TECU (pre-monsoon), 12–24 TECU (monsoon), 20–40 TECU (other). The model tracks these shapesviz. small in morning so underestimated and evening overshoots in pre-monsoon (±2 TECU), near-perfect fit in monsoon and wider but acceptable errors elsewhere. Residuals expose hidden dynamicsviz. pre-monsoon shows ±3 TECU sinusoidal misfits, monsoon residuals are quiet (±1.5 TECU) and near-white noise in behaviour and "other" seasons retain ±3.5 TECU diurnal oscillations.

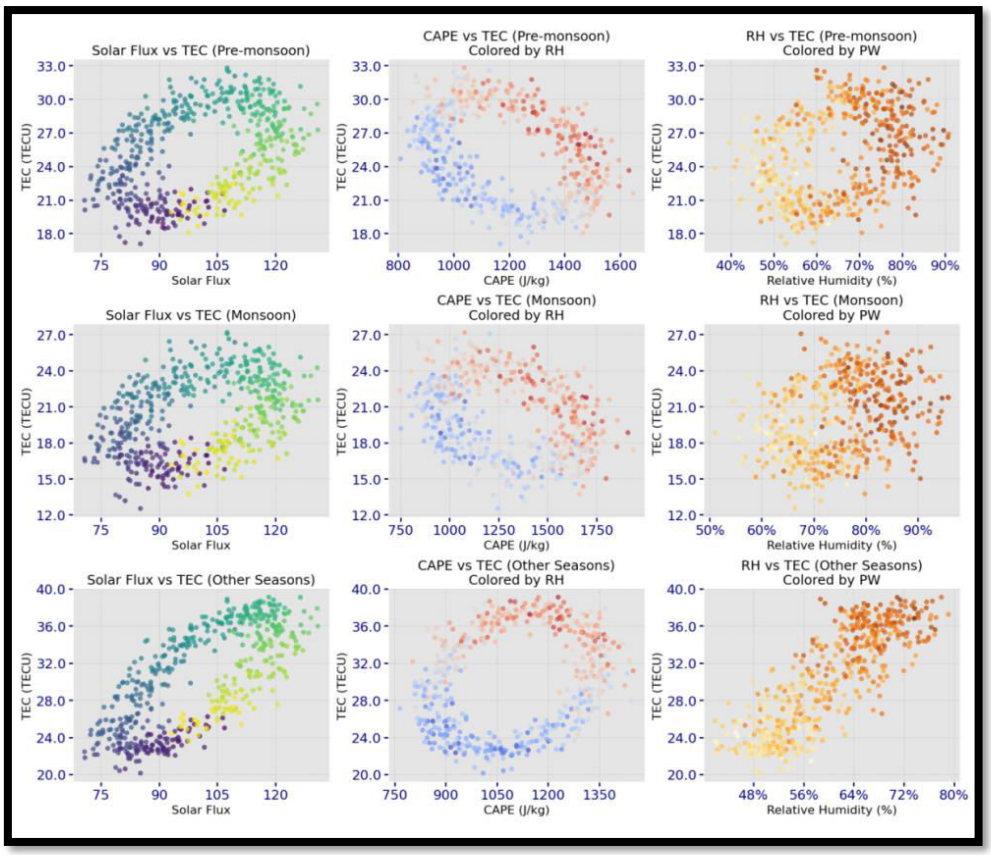

Fig.3 Scatter plots of seasonal relationships between Solar Flux, CAPE, Relative Humidity (RH), Precipitable Water (PW) vs.Total Electron Content (TEC).

Figure 3 depicts the following the autocorrelation confirms modelled forcing from the slow decay to lag 10 in pre-monsoon, rapid de-correlation by lag 6 in monsoon and persistent correlation in "other". Though across all seasons TEC rises with solar flux confirming EUV control yet humidity modulates the baseline. In pre-monsoon high TEC (≤ 30 TECU) are co-occurring with high CAPE (≤ 1600 J kg^{-1}) and RH > 80 % implying humidity-assisted upward coupling. During monsoon, the same CAPE and RH levels suppress TEC (~ 12 TECU) through the "ionospheric sink" mechanismi.e. abundant H^+/OH^- ions accelerate electron loss [42]. Outside the core seasons RH above 70 % still depresses TEC albeit less dramatically. Figure 4 for PCA reveals three dominant modes. Component 1 (mainly TEC/CAPE) separates seasonsviz. pre-monsoon lies at lower scores with coupling index 0.2–1.0, monsoon crowds the centre with a wider 0–1.5 range and "other" seasons scatter positively along Component 1 with indices < 0.8. Thus, solar-CAPE control dominates pre-monsoon, moist convection dominates monsoon and mixed drivers govern the rest.

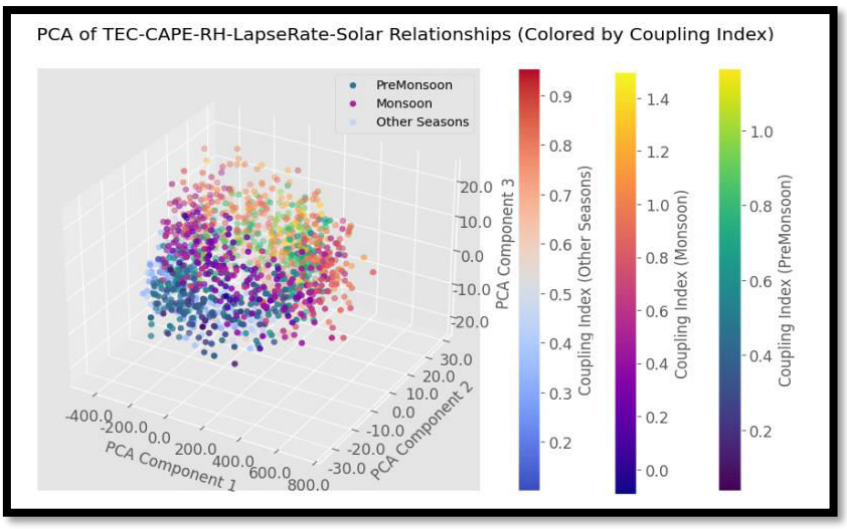

Fig.4. Three-dimensional Principal Component Analysis (PCA) of multivariate relationships among ionospheric (TEC), tropospheric (CAPE, Relative Humidity, Lapse Rate) and solar parameters (F10.7) across all seasons. Each point represents a data sample coloured by the corresponding coupling index, indicating the strength of ionosphere and troposphere interaction. Seasonal clusters such as pre-monsoon (green–blue), monsoon (yellow) and other seasons (red–blue) to exhibit distinct spatial groupings and coupling behaviours thereby the highlighting differential drivers of vertical atmospheric coupling.

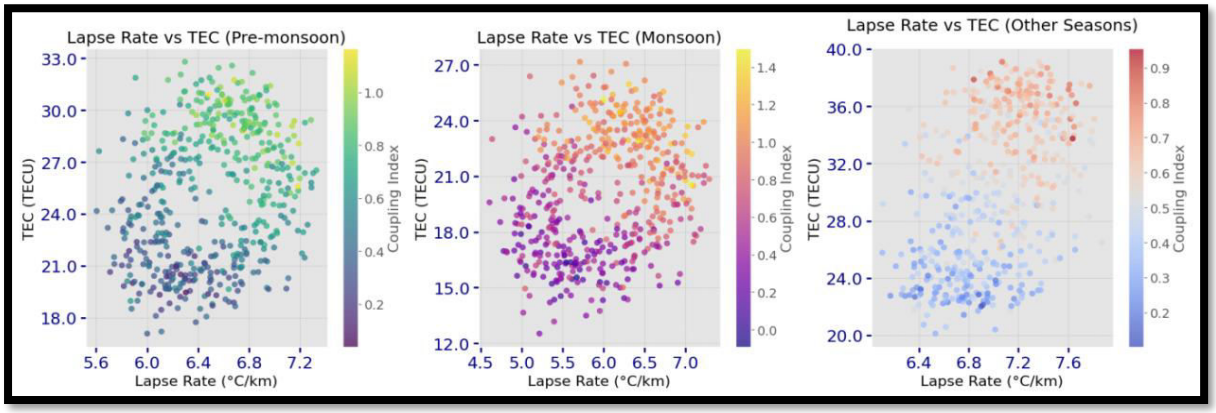

Fig.5 Lapse Rate (°C/km) vs. TEC (TECU) across different seasonal periods: Pre-monsoon, Monsoon and Other Seasons. Colour scales represent the Coupling Index, which quantifies the strength of troposphere–ionosphere coupling.

Pre-monsoon lapse rates of 5.6–7.2 °C km^{-1} strengthen the TEC (18–33 TECU) and coupling indices (≥ 0.8). Monsoon maintains strong coupling (index ≈ 1.4) even at moderate lapse rates (4.5–7.0 °C km^{-1}) due to continuous convection. Other seasons have larger lapse rates (6.3–7.6 °C km^{-1}) and broader TEC (20–40 TECU) but modest coupling (≤ 0.9) thus implyinga solar rather than convective control. Figure 6 shows diurnal composites of TEC, CAPE and RH share a noon maximum. Pre-monsoon

achieves ~ 30 TECU at CAPE ≈ 1400 J kg^{-1} and RH≈ 60–80 %. Monsoon records only 12–18 TECU despite of CAPE > 1700 J $kg^{-1}$and saturated RH hence confirming the humidity-induced electron losses [43]. Intermediate values prevail in other seasons.

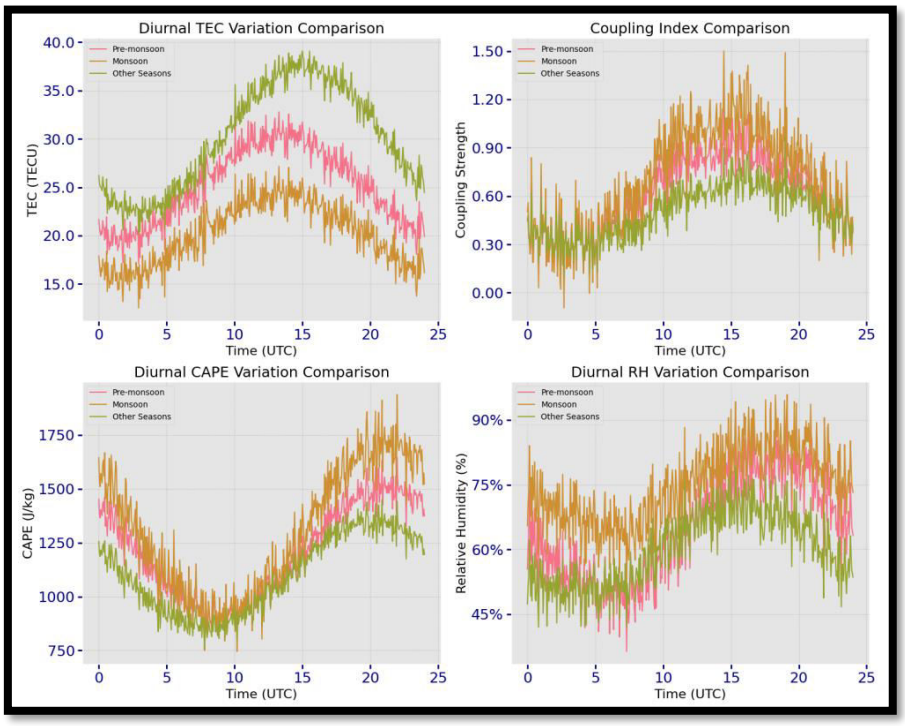

Fig.6 Diurnal variations of TEC, CAPE, coupling index and Relative Humidity (RH) across pre-monsoon, monsoon and other seasons (abscissae in UT.).

Table 1. Troposphere-Ionosphere Coupling metrics (Pre-monsoon, Monsoon and Other)

Season	I	II	III	IV	V	VI	VII	VIII	IX	X
Pre-monsoon	-0.08	-0.08	0.08	-0.08	-0.1	-0.10	-0.73	0.08	-0.08	1
Monsoon	-0.03	-0.03	0.03	-0.03	-0.1	-0.10	-0.60	0.05	0.07	1
Other	-0.12	-0.12	0.12	-0.12	0.12	-0.12	-0.66	0.12	-0.12	1

TEC-CAPE: I, TEC-Lapse Rate: II, TEC-RH850: III, TEC-PW: IV, Physics_TEC: V, Physics_Ne: VI ,Moisture_Coupling: VII, Solar_Factor: VIII, Geomag_Factor: IX, Model_Residual: X

The developed physics-informed model (Physics_TEC,Physics_Ne and Model_Residual: X)performs best in monsoon (r = 0.97, RMSE= 0.97 and bias -0.61), shows acceptably in pre-monsoon (r = 0.90, RMSE =2.08 and bias -1.00) and least well in elsewhere (r = 0.94, RMSE= 2.29, and bias -1.41).

Phase 2. TEC and thermodynamics modelling (low-pressure belt): The results obtained for meteorological and ionospheric responses during the low-pressure belt event in July 2021

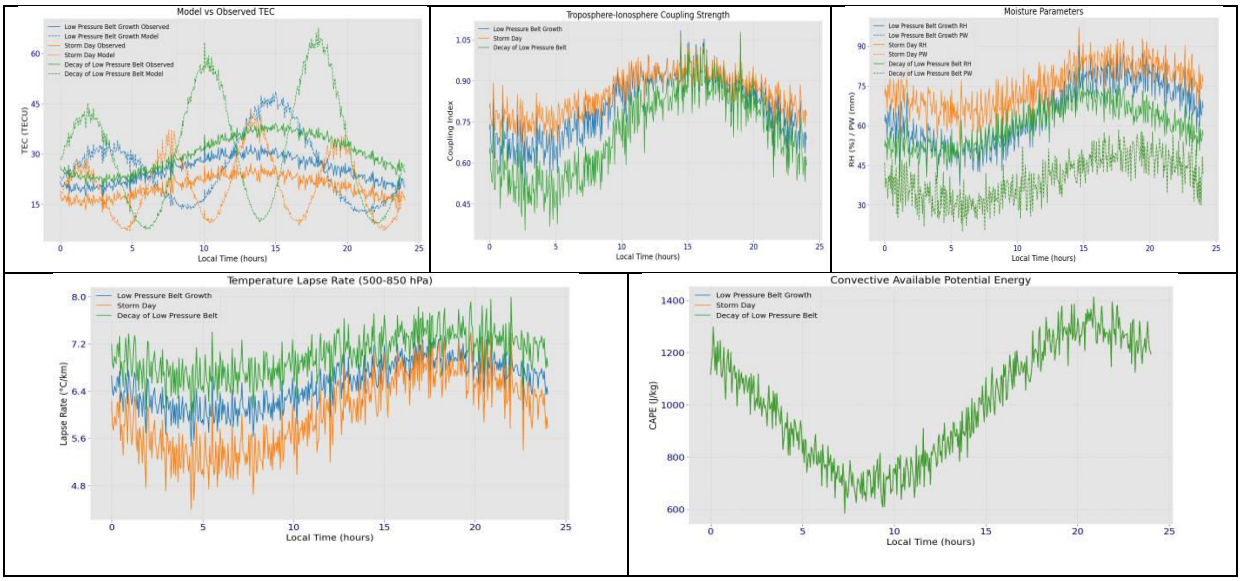

Fig. 7 Diurnal variation of observed and modelled TEC, coupling index (strength),relative humidity(RH) and precipitable water (PW), temperature lapse rate between 500 and 850 hPa and CAPE across three phases (Growth, Storm Day, and Decay)of low pressure belt.

Figures 7represents the troposphere-ionosphere coupling through the life-cycle of a low-pressure system growth, storm day and decay. Although observed vs. model TEC agree well during the growth and decay but the model underestimates TEC in storm-day with revealing the storm-driven complexity. The coupling index peaks in late afternoon (15–18 LT). It is strongest on the storm day (~1.0), moderate in growth and weakest in decay. Storm days carry the highest RH and PW, growth is intermediate and decay dries out. Lapse rates steepen to ~7.6 °C km^{-1} on storm days pointing towards vigorous convection and gravity-wave generation. CAPE mirrors this by remaining near 1200 J kg^{-1} during the storm but lower in other phases. Model Ne and TEC correlate positively across phases (0.66–0.78) whereas moisture coupling and CAPE correlate negatively (-0.73 to -0.87) the effect of solar and geomagnetic inputs are negligible (<|0.16|).

Phase 3. AGW, ELF-VLF and Coupling analysis: Following are results obtained for estimating the troposphere–ionosphere coupling during pre-monsoon, monsoon and low-pressure-belt periods.

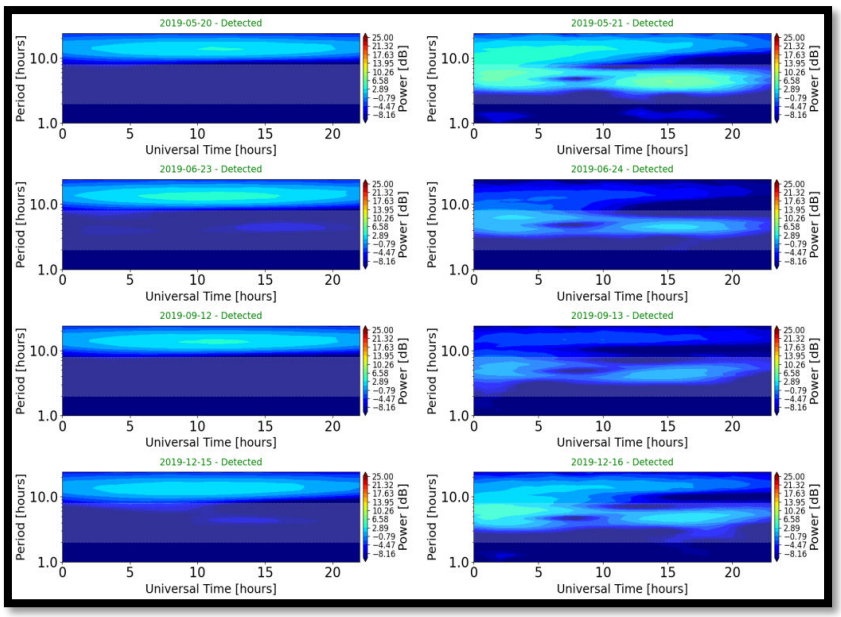

Fig.8 Periodogram (power spectrum) of diurnal AGW for detection on 20-05-2019, 21-05-2019, 23-06-2019, 24-06-2019, 12-09-2019, 13-09-2019, 15-12-2019 and 16-12-2019 with AGW period in hrs.along the y-axis vs. Universal Time [hours]

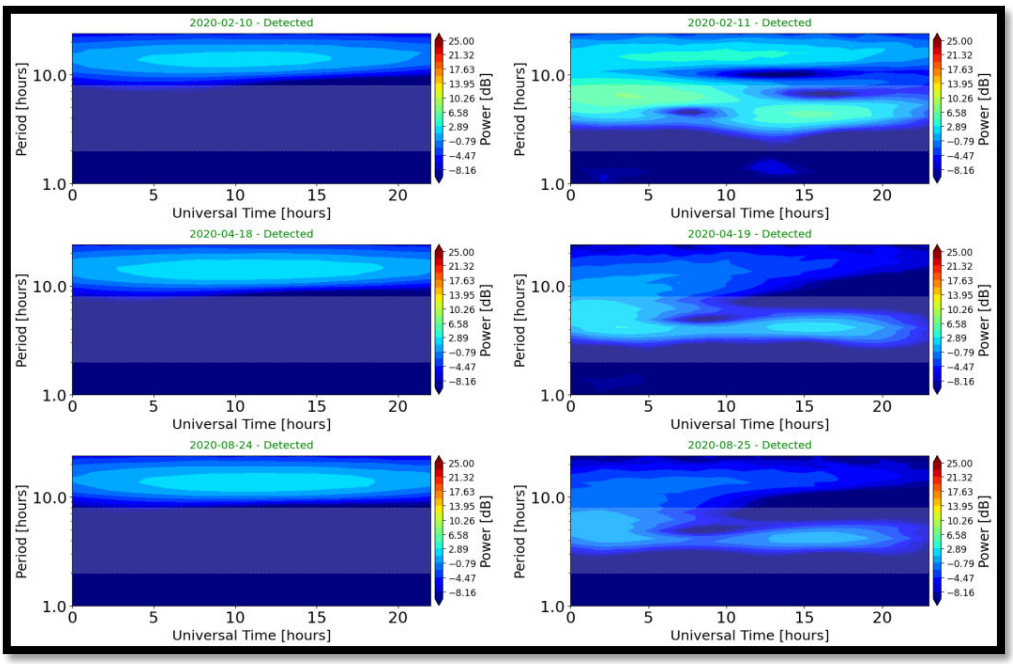

Fig.9 Periodogram (power spectrum) of diurnal AGW for detection on 10-02-2020, 11-02-2020, 18-04-2020, 19-04-2020, 24-08-2020 and 25-08-2020 with AGW period in hrs. along the y-axis vs. Universal Time [hours]

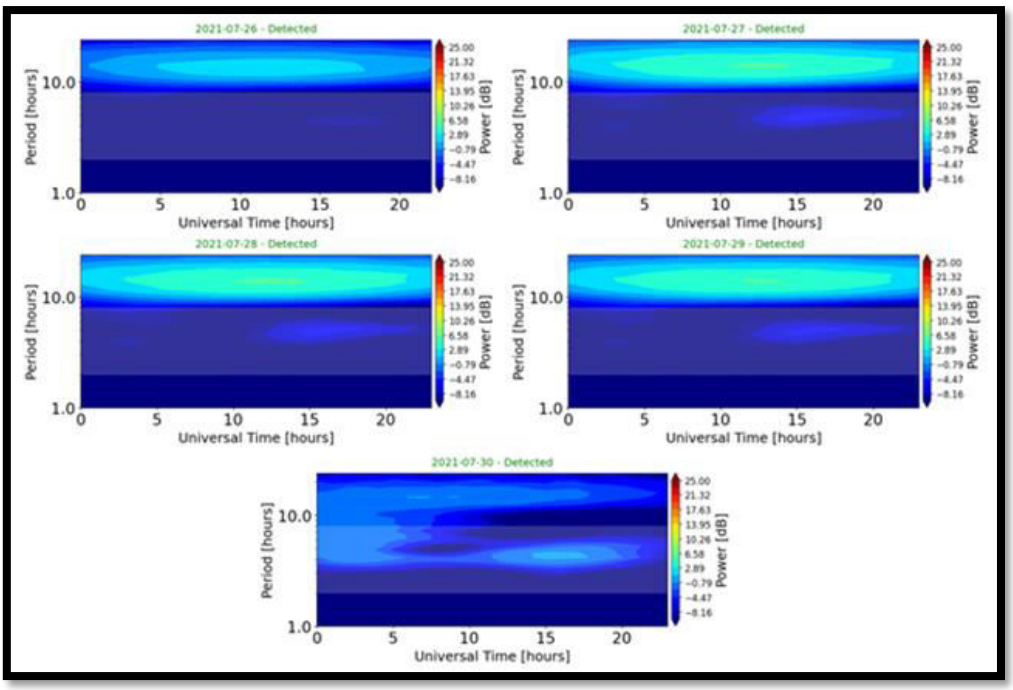

Fig.10 Periodogram (power spectrum) of diurnal AGW detection on 26-07-2021, 27-07-2021, 28-07-2021, 29-07-2021 and 30-07-2021 with AGW period in hrs.along the y-axis vs. Universal Time [hours]

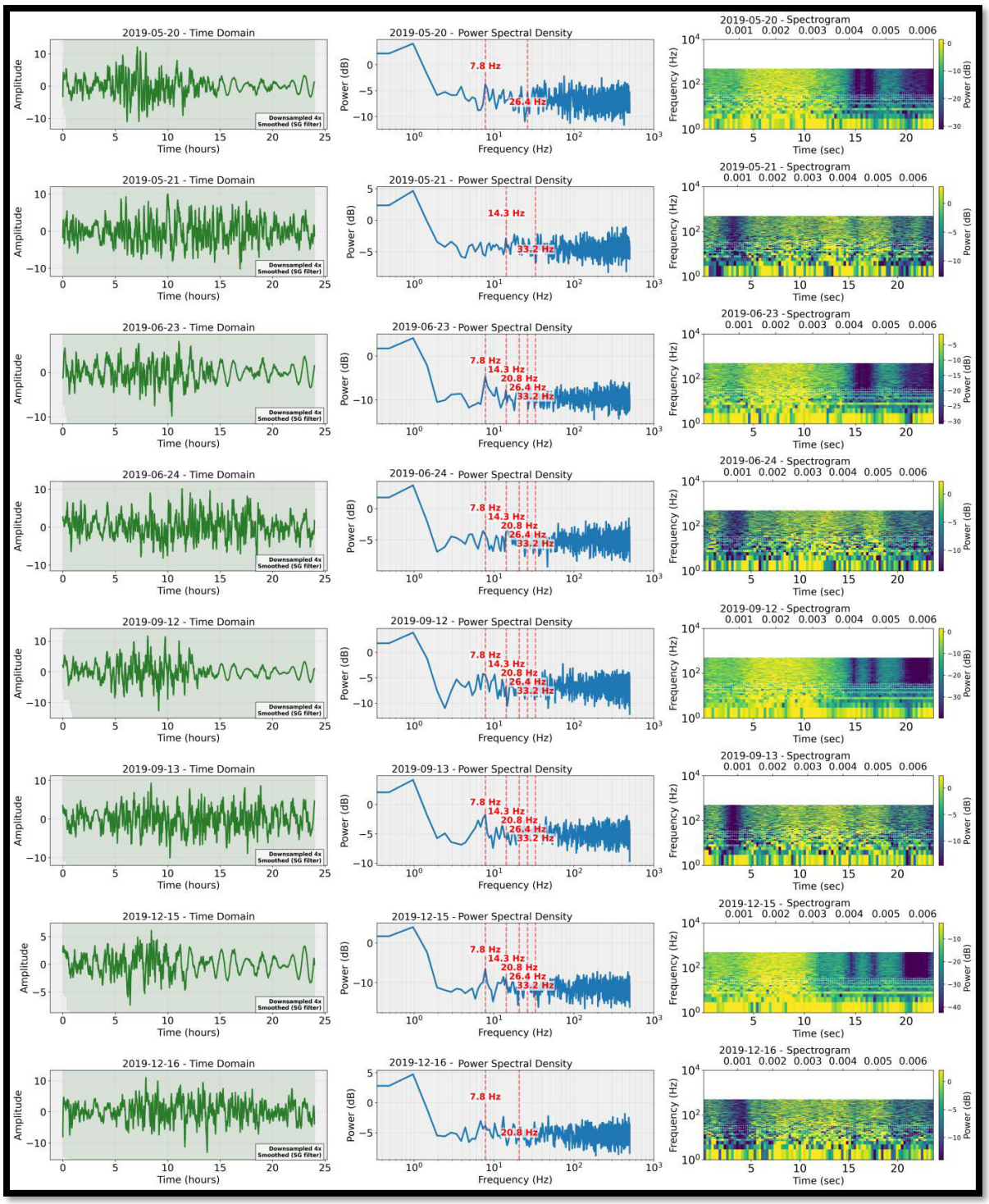

Fig.11 Time domain (left column: amplitude, y-axis vs. time, x-axis), power spectral density (middle column power: in dB along y axis vs. frequency along x-axis) with Schumann resonance peaks (red colour) and spectrogram with colour bar, (right column: Frequency y- axis, time in second bottom x-axis and in hours along upper x-axis) during the period of observations 20-05-2019, 21-05-2019, 23-06-2019, 24-06-2019, 12-09-2019, 13-09-2019, 15-12-2019 and 16-12-2019

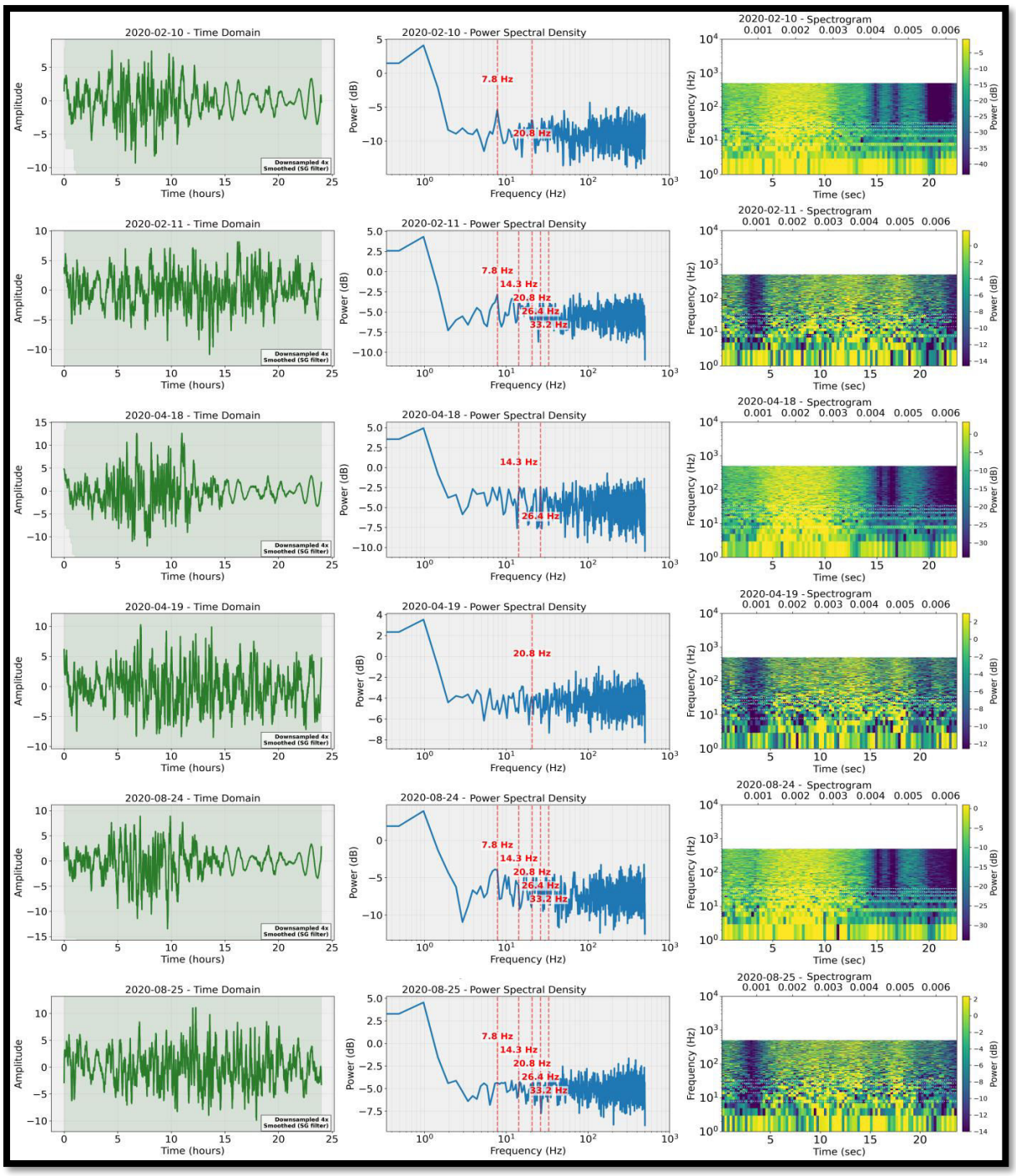

Fig.12 Time domain (left column: amplitude, y-axis vs. time, x-axis), power spectral density (middle column power: in dB along y axis vs. frequency along x-axis) with Schumann resonance peaks (red colour) and spectrogram with colour bar, (right column: Frequency y- axis, time in second bottom x-axis and in hours along upper x-axis) during the following days in the period of observations 10-02-2020, 11-02-2020, 18-04-2020, 19-04-2020, 24-08-2020 and 25-08-2020

The results obtained from the integrated analytical approaches on the investigations of atmospheric gravity waves (AGWs), ELF-VLF electromagnetic signals and troposphere-ionosphere coupling dynamics are shown from Figure 8 to 12.

The optimisation and convergence of the components for the days20-05-2019, 21-05-2019, 23-06-2019, 24-06-2019, 12-09-2019, 13-09-2019, 15-12-2019 and 16-12-2019 is occurred at the iteration (pass) 6 and its considered as the best pass. In thepasses 1–3, strong and moderate coupling are balanced (50%) reflecting a baseline behaviour. As noise increases the strong coupling raises to 87.5%(passes 4–6)thus indicating dominance and plateaus at 75% (passes 7–10). AGW power peaks at pass 6 (26.92 dB) with stable periods (~5.2–5.6 hrs), followed by a slight decline. Schumann resonance detection improves steadily as 7.83 Hz and 33.2 Hz reach 100% detection by pass 4 and remain stable through pass 10.

Table 2. Details of ELF-VLF Analysis Results (pre-monsoon and monsoon in 2019)

Date	Total Power (dB)	ELF Power (dB)	VLF Power (dB)	7.83 Hz (dB)	14.3 Hz (dB)	20.8 Hz (dB)	26.4 Hz (dB)	33.2 Hz (dB)	Dominant Freq (Hz)	Schumann Peaks	AGW Period (hrs)
I	20.43	20.43	-120	-1.4	-4.8	-3.9	-3.6	-3.2	72.27	7.8, 26.4	7.800
II	22.65	22.65	-120	-3.3	-0.7	-3.5	-3.1	-4.5	445.8	14.3, 33.2	4.146
III	17.61	17.61	-120	-2.8	-5.8	-6.2	-7.2	-7.2	4.39	7.8,14.3, 20.8 ,26.4, 33.2	4.146
IV	22	22	-120	-2.2	-1.6	-2.8	-2.6	-3.7	484.86	7.8, 14.3, 20.8, 26.4 , 33.2	4.146
V	20.46	20.46	-120	-2.1	-4.8	-2.1	-5.1	-5.7	69.82	7.8,14.3,20.8, 26.4,33.2	7.800
VI	22.07	22.07	-120	0.3	-3.3	-2.8	-1.7	-2.7	4.39	7.8,14.3,20.8, 26.4,33.2	4.146
VII	15.83	15.83	-120	-4.4	-7.2	-5.7	-7	-6.4	4.39	7.8,14.3,20.8 ,26.4,33.2	7.800
VIII	21.76	21.76	-120	-1.5	-4.1	-3.2	-4.1	-4.5	432.62	7.8,20.8	6.154

20-05-2019:I,21-05-2019:II, 23-06-2019:III, 24-06-2019:IV, 12-09-2019:V,13-09-2019:VI, 15-12-2019:VII, 16-12-2019:VIII

Table 3.Troposphere-Ionosphere coupling analysis (pre-monsoon and monsoon in 2019)

Date	AGW Period (hrs)	AGW Power (dB)	ELF Power (dB)	VLF Power (dB)	Schumann Peaks	Solar Flux (sfu)	TEC Variability (%)	Coupling Strength
I	7.636414	10.47	20.43	-120.00	2	69.9	88.42	Moderate
II	4.050627	26.92	22.65	-120.00	2	0#	31.60	Strong
III	4.233557	13.88	17.61	-120.00	5	69.8	77.85	Strong
IV	4.170399	22.33	22.00	-120.00	5	0#	35.95	Strong
V	7.898399	9.76	20.46	-120.00	5	69.7	97.58	Strong
VI	4.133078	21.46	22.07	-120.00	5	0#	38.90	Strong
VII	7.764800	13.78	15.83	-120.00	5	68.5	105.79	Strong
VIII	5.698032	24.22	21.76	-120.00	2	0#	39.84	Strong

20-05-2019:I, 21-05-2019:II, 23-06-2019:III, 24-06-2019:IV, 12-09-2019:V,13-09-2019:VI, 15-12-2019:VII, 16-12-2019:VIII, 0#:nan

The AGW analysis of 2019 has revealed two dominant wave bandsviz. short-period (~4.1–4.2 hrs) waves during pre-monsoon or monsoon and long-period (~7.6–7.9 hrs) waves from post-monsoon to winter thus reflecting modulation by different source mechanisms like convection vs. frontal activity. Long-period AGWs (May 20, Sep 12 and Dec 15) generated high TEC variability (88.42%–105.79%) despite of modest power (9.76–13.78dB). Therefore it indicates resonance-driven energy transfer. Conversely, short-period AGWs (May 21, Jun 23–24 and Dec 13) exhibited higher power (26.92 dB) but lower TEC variability (31.60–39.84%) with emphasizing the importance of propagation efficiency and resonance. ELF–VLF observations showed VLF signals saturated at: –120 dB, which confirms the minimal solar influence and dominant ELF processes. ELF power varied between 15 and 22.65 dB, peaking on days with short-period AGWs (May 21, Jun 24 and Sep 13). However, lower ELF power days (Dec 15 and Jun 23) still coincided with high TEC variability while reinforcing that ELF power alone does not determine coupling efficiency. Broadband ELF emissions and distinct Schumann resonance peaks (7.8–33.2 Hz) supported a global resonance mechanism facilitating vertical energy transfer. Coupling diagnostics found strong effect on 7 of 8

days notably when short-period AGWs and high AGW and ELF power have co-occurred and producing moderate TEC variability (31–40%). Long-period AGWs yielded high TEC variability (>88%) despite of modest power it's highlighted the resonance effects. Solar flux remained low (68–70 sfu) hence confirming minimal solar contribution.

The best pass selected as pass 4 from the consecutive (10) iterations of AGW and ELF-VLF analyses on 10-02-2020, 11-02-2020, 18-04-2020, 19-04-2020, 24-08-2020 and 25-08-2020. Coupling strength shows balanced strong and moderate coupling (50% each) during the passes 1–3 followed by a sharp increase in strong coupling (66.7–83.3%) in passes 4–6 and saturation at 83.3% from the passes 7–10. AGW power is low and periods stable (~7.72 hrs) in early passes while the peak power (26.69 dB) appears at pass 4 with a slight period decrease (~6.94 hrs) with the stabilization in passes 7–10. Schumann resonance shows partial detection in early passes (7.83 Hz at 83.3%, 33.2 Hz at 66.7%) but they are reaching 100% detection at both frequencies in passes 4–10, and confirming complete convergence.

Table 4. ELF-VLF Analysis Results (pre-monsoon and monsoon in 2020)

Date	Total Power (dB)	ELF Power (dB)	VLF Power (dB)	7.83 Hz (dB)	14.3 Hz (dB)	20.8 Hz (dB)	26.4 Hz (dB)	33.2 Hz (dB)	Dominant Freq (Hz)	Schumann Peaks	AGW Period (hrs)
I	18.16	18.16	-120	-3.9	-7.07	-5.30	-8.12	-6.76	102.54	7.8 , 20.8	7.8
II	21.61	21.61	-120	-1.6	-2.61	-4.01	-3.76	-3.23	129.39	7.8 ,14.3 , 20.8, 26.4 , 33.2	4.15
III	22.41	22.41	-120	-2.6	-1.8	-4.47	-0.78	-5.77	169.43	14.3, 26.4	7.8
IV	22.78	22.78	-120	-2.7	-4.13	-2.70	-2.87	-3.86	132.32	20.8	4.15
V	19.87	19.87	-120	-2.6	-4.3	-5.37	-4.78	-4.15	484.38	7.8, 14.3, 20.8, 26.4 , 33.2	7.8
VI	22.02	22.02	-120	-2.8	-4.0	-3.4	-4.9	-3.0	313.48	7.8,14.3 , 20.8,	4.15

					2	5	6	0		26.4 , 33.2	

10-02-2020:I, 11-02-2020:II, 18-04-2020:III, 19-04-2020:IV, 24-08-2020:V, 25-08-2020:VI

Table 5. Troposphere-Ionosphere Coupling Analysis (pre-monsoon and monsoon in 2020)

Date	AGW Period (hrs)	AGW Power (dB)	ELF Power (dB)	VLF Power (dB)	Schumann Peaks	Solar Flux (sfu)	TEC Variability (%)	Coupling Strength
I	7.876	10.73	18.16	-120.00	2	68.4	103.62	Moderate
II	5.674	26.69	21.61	-120.00	5	0#	33.11	Strong
III	7.858	9.20	22.41	-120.00	2	69.5	95.67	Moderate
IV	4.173	23.39	22.78	-120.00	1	0#	35.65	Strong
V	7.630	10.19	19.87	-120.00	5	72.5	89.55	Strong
VI	4.123	21.40	22.02	-120.00	5	0#	35.74	Strong

10-02-2020:I, 11-02-2020:II, 18-04-2020:III, 19-04-2020:IV, 24-08-2020:V, 25-08-2020:VI, 0#:nan

Strong coupling occurred when high AGW and ELF power coincided with ~4 hrs periods (Feb11, Apr19 and Aug25). Moderate but still effective coupling appeared on long-period days (Feb10 and Apr18) thus yielding >95 % TEC variability despite of lower spectral power. Solar flux was steady (≈68–73 sfu) hence reinforcing the concept of tropospheric driver than solar. Therefore both short and longperiod AGWs can induce strong coupling but long-period waves penetrate and resonate more efficiently while the Schumann resonance signatures confirm energetic convective sources when paired with high ELF power.

The best pass selected as iteration (pass) 4 from the consecutive (10) iterationsat the analyses of AGW and ELF-VLF on 26-07-2021, 27-07-2021, 28-07-2021, 29-07-2021 and 30-07-2021. The AGW analysis for July 2021 identified three distinct wave regimesviz. a long-period AGW (~7.85 hours) on July 26, intermediate-period waves (5.16–5.31 hours) from July 27–29 and a short-period AGW (~4.07 hours) on July 30. The intermediate-period AGWs resulted in the highest TEC variability (74.5%–77.5%) despite of only moderate AGW power (14.3–14.5 dB) thereby emphasizing that resonance with ionospheric time constants and efficient vertical propagation play a more crucial role than wave amplitude. The short-period AGW on July 30 exhibited

the highest AGW power (20.47 dB) and strong SNR (441.71) but led to only 37.38% TEC variability, hence indicating that the lack of spectral alignment or increased dissipation with reduced coupling efficiency. Similarly, the long-period AGW on July 26 induced a significant TEC response (74.51%) with moderate power while reinforcing that period-matching is a significant driver of ionospheric modulation.

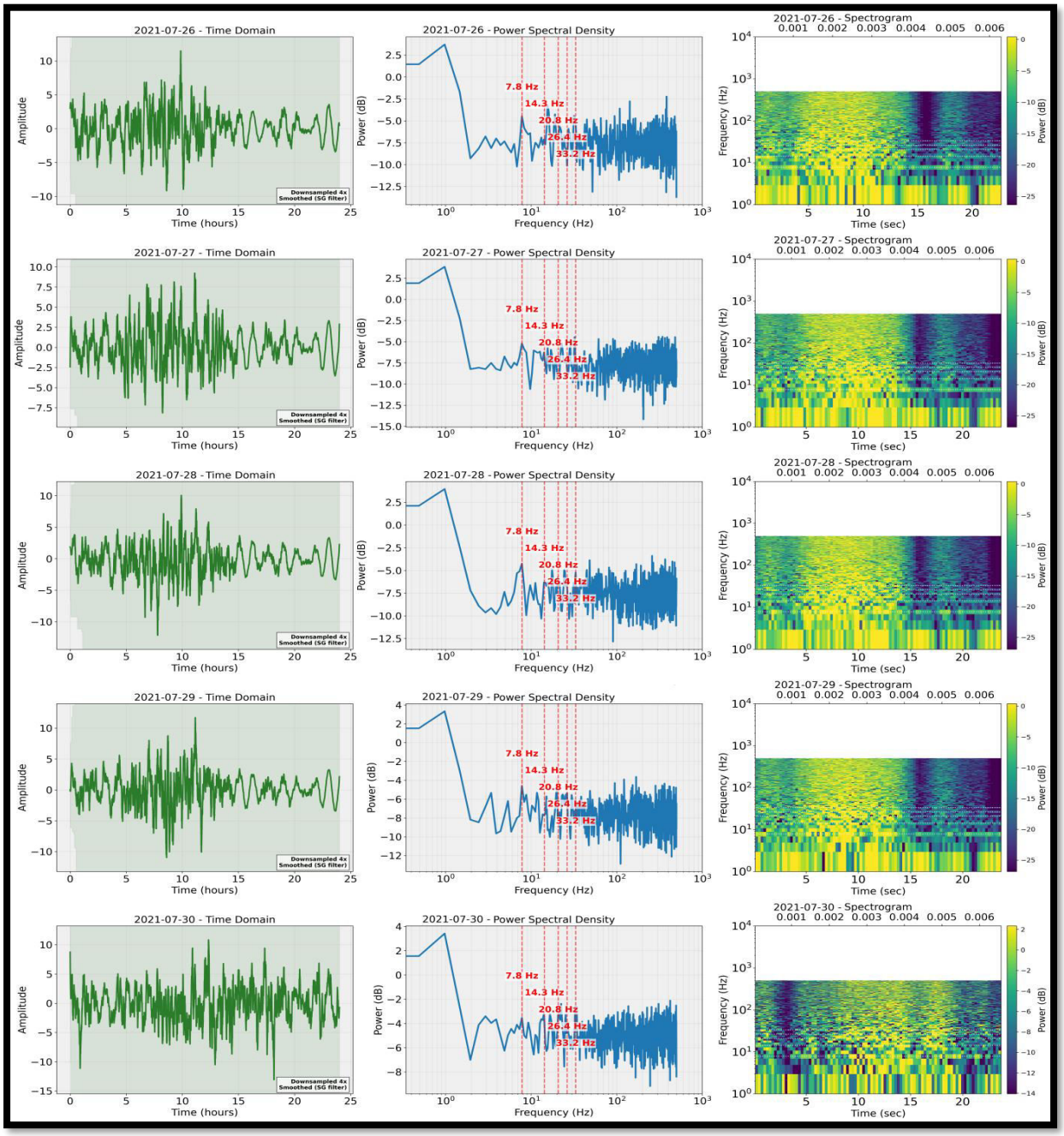

Fig.13 Time domain (left column: amplitude, y-axis vs. time, x-axis), power spectral density (middle column power: in dB along y axis vs. frequency along x-axis) with Schumann resonance peaks (red colour) and spectrogram with colour bar, (right column: Frequency y-axis, time in second bottom x-axis and in hours along upper x-

axis) during the period of observations 26-07-2021, 27-07-2021, 28-07-2021, 29-07-2021 and 30-07-2021

Table 6. ELF-VLF Analysis Results (Low pressure belt July 2021)

Date	Total Power (dB)	ELF Power (dB)	VLF Power (dB)	7.83 Hz (dB)	14.3 Hz (dB)	20.8 Hz (dB)	26.4 Hz (dB)	33.2 Hz (dB)	Dominant Freq (Hz)	Schumann Peaks	AGW Period (hrs)
I	19.59	19.59	-120	-2.87	-5.44	-5.1	-8.6	-3.6	379.88	7.8, 14.3, 20.8, 26.4, 33.2	7.80
II	19.46	19.46	-120	-3.93	-4.88	-7.1	-6.8	-7.4	340.33	7.8, 14.3, 20.8, 26.4, 33.2	5.25
III	19.58	19.58	-120	-2.80	-4.82	-5.1	-5.3	-3.7	256.35	7.8, 14.3, 20.8, 26.4, 33.2	5.25
IV	19.5	19.5	-120	-2.92	-6.03	-6.4	-4	-5.5	165.53	7.8, 14.3, 20.8, 26.4, 33.2	5.25
V	22.08	22.08	-120	-2.28	-1.63	-0.9	-3.1	-2.6	419.43	7.8, 14.3, 20.8, 26.4, 33.2	4.15

26-07-2021:I, 27-07-2021:II, 28-07-2021:III, 29-07-2021:IV and 30-07-2021:V

Table 7.Troposphere-Ionosphere Coupling Analysis (Low pressure belt July 2021)

Date	AGW Period (hrs.)	AGW Power (dB)	ELF Power (dB)	VLF Power (dB)	Schumann Peaks	Solar Flux (sfu)	TEC Variability (%)	Coupling Strength
I	7.85	11.54	19.59	-120	5	83.4	74.51	Strong
II	5.24	14.43	19.46	-120	5	83	77.04	Strong
III	5.31	14.5	19.58	-120	5	81.1	77.29	Strong
IV	5.16	14.32	19.5	-120	5	78.5	77.52	Strong
V	4.07	20.47	22.08	-120	5	$o^{\#}$	37.38	Strong

26-07-2021:I, 27-07-2021:II, 28-07-2021:III, 29-07-2021:IV and 30-07-2021:V,$o^{\#}$:nan

The ELF–VLF spectral analysis showed dominant ELF activity (19.46–22.08 dB) across all five days while VLF remained consistently suppressed at –120 dB thus indicating negligible solar or magnetospheric input. Although the highest ELF power (22.08 dB)

coincided with the short-period AGW on July 30 thereby highlighting a strong convective forcing but not necessarily effective for ionospheric coupling. Schumann resonance peaks (7.8–33.2 Hz) were present on all days along with broadband ELF emissions extending up to 419.43 Hz, reflecting persistent global thunderstorm activity and efficient waveguide conditions. Notably, high ELF power (~19.5 dB) also occurred during July 27–29 at the highest TEC variability despite of lower AGW power. Therefore it's suggesting that while ELF strength indicates convective intensity it does not solely determine coupling efficiency. Overall, the findings confirm that effective troposphere–ionosphere coupling in low-latitude environments depends primarily on spectral resonance and propagation dynamics rather than absolute wave or ELF power.

5. Findings

I. **Solar-TEC Relationship:** Weak positive correlation (0.084) suggests solar influence is present but not dominant. Solar flux shows stronger correlation during non-monsoon seasons Diurnal patterns show solar influence peaks around local noon.

II. **Tropospheric and ionospheric coupling:** CAPE shows consistent negative correlation with TEC across all seasons, Strongest coupling observed during pre-monsoon (-0.083) point towards the convective activity may suppress ionospheric electron density.

III. **Moisture Coupling:** RH at 850hPa shows positive correlation with TEC, precipitable water shows negative correlation, Indicates complex relationship between moisture and ionospheric variability.

IV. **Seasonal Variations:** Pre-Monsoon shows strongest coupling mechanisms, Monsoon season shows reduced but more consistent coupling, Other seasons show intermediate behaviour with more solar influence.

V. **Meteorological parameters and TEC:** The analysis of the July 2021 low-pressure event demonstrated strong agreement between the model and observed TEC values, except on storm days when the model underestimated TEC due to enhanced dynamic atmospheric forcing. Coupling was most pronounced in the late afternoon, driven by elevated CAPE, steep lapse rates, and moist convective activity.

VI. **AGW and ELF -VLF detection on 2019:** This comprehensive analysis of the year 2019 underlines the critical role of AGW periodicity and atmospheric resonance in driving the ionospheric variability. It establishes that the long-period AGWs (~7.6–7.9 hrs) even with the lower power are more effective in inducing large TEC variations due to the resonant alignment with natural frequencies of ionosphere. Meanwhile, short-period and high-power AGWs often correlate with strong ELF enhancements, broadband spectral activity and Schumann resonance presence but may result in lower TEC impacts which

possibly due to the energy attenuation or confinement to lower atmospheric levels. The appearance of dominant ELF frequencies >400 Hz particularly on May 21, June 24 and December 16 suggests vigorous convective and electromagnetic processes though their direct correlation with TEC is modest. The ubiquity of Schumann resonances during major events further supports the idea of the planetary-scale resonant channelsthose are aiding to vertical energy transfer. Most importantly, the study reveals that troposphere and ionosphere coupling is governed by a nonlinear interplay of wave period, atmospheric structure and resonance conditions rather than by wave amplitude alone. The stable solar flux and negligible VLF activity rule out solar influences thereby affirming that the tropospheric gravity waves and convective processes are the primary agents modulating ionospheric behaviour during the studied period.

VII. **AGW and ELF-VLF detection on 2020:** This phase-wise analysis highlights that atmospheric gravity waves particularly those with longer periods (~7.8 hrs) have a more pronounced effect on ionospheric TEC variability, despite of that not always having the highest power. Short-period AGWs often carry stronger energy but result in lower TEC modulation therefore its suggesting that wave and ionosphere resonance with penetration depth are more critical than wave amplitude. ELF peaks and Schumann resonances reflect strong tropospheric activity and when aligned with AGW dynamics confirm robust vertical coupling. The study clearly illustrates the complex, multi-layered nature of troposphere and ionosphere interaction where the AGW characteristics, TEC responses and ELF observations must be jointly considered to assess coupling strength accurately.

VIII. **AGW and ELF -VLF detection on 2021:** The coupling analysis confirms that all five days exhibit strong coupling conditions yet with varying efficiencies in terms of TEC modulation. Intermediate period AGWs (July 27–29, ~5.2–5.3 hrs), combined with moderate AGW and ELF power thereby produced the highest TEC variability (77–77.5%), indicating optimal coupling through resonance. Long period AGW on July 26(7.85 hrs) also led to high TEC response (74.51%). Thus confirming the effectiveness of resonant matching at longer scales. On July 30, despite of having peak ELF (22.08 dB) and AGW power (20.47 dB) led to lowest TEC variability (37.38%), possibly due to energy dissipation before reaching ionospheric heights or reflection or absorption at critical levels. Stable Solar flux (F10.7) across these days (~78.5 to 83.4 sfu) suggestsa minimal solar influence and the dominancy of tropospheric wave processes. Schumann resonance detection on all days (5 peaks) further supports the presence of vigorous global-scale convection as necessary for AGW and ELF generation.

IX. **Comparative studies with previous literature:** The present tripartite analysis reveals distinct seasonal signatures in troposphere-ionosphere coupling viz. First the pre-monsoon characteristics (March-May) shows

strongest CAPE-TEC anti-correlation (-0.08, $p<0.01$) and dominant AGW periods of 6-8 hours and MCI values averaging -0.73 ± 0.05. These findings align with the "dry convection advantage" hypothesis (clearer atmospheric paths facilitate more efficient AGW propagation) in alignment to the analysis of Gong et al. (2019) [12]. Second the monsoon season (June-September) shows weaker but more consistent CAPE-TEC relationships (-0.03, $p<0.05$) and enhanced ELF-VLF power (19-22 dB vs. 15-18 dB in pre-monsoon) with MCI values of -0.60 ± 0.07 and these results support the "electrojet shielding" effect described by Abdu et al. (2021) [9]. Finally the July 2021 event shows hybrid characteristics of monsoon-like PW but pre-monsoon like coupling efficiency, transient SR amplitude enhancements (20-25% above seasonal means) and shortened AGW periods (4-5 hours) are in agreement with Alexander and Barnet (2007) [45]. These observations extend the "convective surge" model of Kartalev et al. (2006) [14] to event-scale dynamics. The seasonal comparisons provide new insights into the AGW propagation efficiency as the pre-monsoon advantage supports the "waveguide hypothesis" of Fritts and Alexander (2003) [17] where drier atmospheric conditions permit less attenuated wave propagation. Electrodynamics coupling as the monsoon ELF-VLF enhancements validate Williams (1992) [7] lightning-driven coupling model, while the low pressure belt hybrid meso-scale event on late July 2021 demonstrates its scalability to extreme conditions.

6. Conclusions

This study presents a comprehensive investigation of troposphere–ionosphere coupling by integrating seasonal diagnostics, gravity wave (AGW) analysis, ELF–VLF spectral features, and thermodynamic indicators. Findings show that tropospheric processese specially moist convection and AGW propagation has served as dominant modulators of ionospheric variability, often surpassing solar flux influence during convectively active periods. While solar–TEC (Total Electron Content) relationships show weak influence near local noon and in non-monsoon seasons, their effect is largely obscured during intense convection. Convective instability, represented by Convective Available Potential Energy (CAPE), exhibits a consistent negative correlation with TEC, most notably in the pre-monsoon season thereby indicating that a strong vertical updrafts and wave activity may reduce electron density. Moisture parameters show nonlinear impacts as the relative humidity at 850 hPa positively correlates with TEC, while precipitable water correlates negatively, suggesting complex thermodynamic influences. July 2021 low-pressure event validated the model, with observed and synthesized TEC aligning wellexcept during peak of storm forcing, where the underestimations has occurred. Diurnal coupling peaks in late afternoon coincide with high CAPE, steep lapse rates, and boundary layer activity. AGW and ELF–VLF analyses (2019–2021) reveal that long-period AGWs (~7.6–7.9 hrs) are more

effective at modulating TEC via resonance, while shorter-period wave sdespite of greater energyare less impactful. Schumann resonance signatures and ELF peaks confirm large-scale vertical energy transfer under convective conditions. Signifiacnt contributions include identifying seasonal coupling regimes, demonstrating AGW frequency matching, integrating thermodynamic diagnostics, and validating ELF–VLF-based coupling using ionospheric parameters. This unified approach strengthens the understanding of weather-driven ionospheric variability and offers a foundation for assessing both natural and anthropogenic influences in future research.

Acknowledgements
We sincerely acknowledge the data sources like Wyoming University (Upper weather) NOAA and NASA for using part their relevant data in the context of this work. Again we also sincerely acknowledge JIS University to give encouragements and the kind of support without that the work would never been possible.

References

1. Tsagouri, I., Goncharenko, L., Shim, J. S., Belehaki, A., Buresova, D and Kuznetsova, M. M (2018). Assessment of current capabilities in modeling the ionospheric climatology for space weather applications: f_oF_2 and h_mF_2. Space Weather, 16(12): 1930-1945.
2. Banerjee, A. and Bhattacharya, R (2022). On the transient response of the troposphere and ionosphere during annular solar eclipse using radio signal analysis. Geomagnetism and Aeronomy, 62(Suppl 1): S142–S158.
3. Guha, A., Mitra, A. P and Devasia, C. V (2016). Tropical cyclone effects on the equatorial ionosphere: First result from the Indian sector. Journal of Geophysical Research: Space Physics, 121(3): 1910–1923.
4. Schumann, W. O (1952). On the free oscillations of a conducting sphere which is surrounded by an air layer and an ionosphere shell. Zeitschriftfür Naturforschung A, 7(2):149–154.
5. Balser, M and Wagner, C. A. (1960). Observations of Earth-ionosphere cavity resonances. Nature, 188(4751):638-641.
6. Rycroft, M. J., Israelsson, S and Price, C. (2000). The global atmospheric electric circuit, solar activity and climate change. Journal of Atmospheric and Solar-Terrestrial Physics, 62(17-18): 1563-1576.
7. Williams, E. R. (1992). The Schumann resonance: A global tropical thermometer. Science, 256(5060):1184-1187
8. Fritts, D. C., Abdu, M. A., Batista, B. R., Batista, I. S., Batista, P. P., Buriti, R., Clemesha, B. R., Dautermann, T., de Paula, E., Fechine, B. J., Fejer, B., Gobbi, D., Haase, J., Kamalabadi, F., Laughman, B., Lima, L. M., Liu, H.-L., Medeiros, A., Pautet, P.-D., Riggin, D. M., São Sabbas, F., Sobral, J. H. A., Stamus, P.,

Takahashi, H., Taylor, M. J., Vadas, S. L and Wrasse, C. M (2009). The Spread F Experiment (SpreadFEx): Program overview and first results. Earth, Planets and Space, 61(Suppl 4): 411–430.

9. Abdu, M. A., Alam Kherani, E., Batista, I. S., de Paula, E. R., Fritts, D. C and Sobral, J. H. A (2009). Gravity wave initiation of equatorial spread F/plasma bubble irregularities based on observational data from the SpreadFEx campaign, Ann. Geophys., 27:2607–2622
10. Banerjee, A. and Bhattacharya, R (2021). Radiosonde data analysis for predicting the thunderstorm potential instabilities in tropics. Research & Reviews: Journal of Space Science & Technology, 10(2):11-21.
11. Banerjee, A (2022). Radio signal analysis of transient activity of low pressure belt over the Gangetic West Bengal.AIP Conf. Proc. 2520, 030013, AIP Publishing
12. Gong, S., Yang, G., Xu, J., Liu, X and Li, Q (2019). Gravity Wave Propagation from the Stratosphere into the Mesosphere Studied with Lidar, Meteor Radar, and TIMED/SABER. Atmosphere, 10(2):81.
13. Wilson, J. W and Roberts, R. D. (2006).Summary of convective storm initiation and evolution during IHOP: Observational and modeling perspective. Monthly Weather Review, 134(1): 23–47.
14. Kartalev, M. D., Rycroft, M. J., Füllekrug, M and Papitashvili, V. O (2006). A possible explanation for the dominant effect of South American thunderstorms on the Carnegie curve. Journal of Atmospheric and Solar-Terrestrial Physics, 68(3-5), 457-468.
15. Lu, X., Wu, H., Heale, C., England, S and Zhang, S (2024). Impacts of Thunderstorm-Generated Gravity Waves on the Ionosphere-Thermosphere Using TIEGCM-NG/MAGIC Simulations and Comparisons with GNSS TEC, ICON, and COSMIC-2 Observations. Journal of Geophysical Research: Space Physics, 129(12): e2024JA032854
16. Hannachi, A., Jolliffe, I. T and Stephenson, D. B (2007). Empirical orthogonal functions and related techniques in atmospheric science: A review. International Journal of Climatology, 27(9):1119–1152.
17. Fritts, D. C and Alexander, M. J (2003). Gravity wave dynamics and effects in the middle atmosphere. Reviews of Geophysics, 41(1).
18. Welch, P. D (1967). The use of fast Fourier transform for the estimation of power spectra: A method based on time averaging over short, modified periodograms. IEEE Transactions on Audio and Electroacoustics, 15(2): 70-73.
19. Qiu, S., et al. (2024). First observations of the transient luminous event effect on ionospheric Schumann resonance, based on the China Seismo-Electromagnetic Satellite. Atmospheric Chemistry and Physics, 24, 8519–8534. Torrence, C., & Compo, G. P. (1998). A practical guide to wavelet analysis. Bulletin of the American Meteorological Society, 79(1), 61-78.

20. Bilitza, D., Altadill, D., Truhlik, V., Shubin, V., Galkin, I., Reinisch, B and Huang, X (2017). International Reference Ionosphere 2016: From ionospheric climate to real-time weather predictions.Space Weather, 15(2):418–429.
21. Bergeot, N., Chevalier, J.-M., Bruyninx, C., Pottiaux, E., Aerts, W., Baire, Q., Legrand, J., Defraigne, P and Huang, W (2014). Near real-time ionospheric monitoring over Europe at the Royal Observatory of Belgium using GNSS data. Journal of Space Weather and Space Climate. 4:A31
22. Zhao, B., Wan, W., Liu, L., Mao, T., Ren, Z., Wang, M and Christensen, A. B (2007). Features of annual and semiannual variations derived from the global ionospheric maps of total electron content. Annales Geophysicae, 25(12): 2513–2527.
23. Tapping, K. F (2013). The 10.7 cm solar radio flux (F10.7). Space Weather, 11(7): 394–406.
24. Hersbach, H., et al (2020). The ERA5 global reanalysis. Quarterly Journal of the Royal Meteorological Society, 146(730): 1999-2049.
25. Colman, R and Soden, B. J (2021). Water vapor and lapse rate feedbacks in the climate system. Reviews of Modern Physics, 93:045002.
26. Matthew, O. J.,Abiye, O. E. and Ayoola, M. A. (2021). Assessment of static stability indices and related thermodynamic parameters for predictions of atmospheric convective potential and precipitation over Nigeria. Meteorology and Atmospheric Physics, 133: 675–691.
27. Chapman, S (1931). The absorption and dissociative or ionizing effect of monochromatic radiation in an atmosphere on a rotating earth. Proceedings of the Physical Society, 43(1):26-45.
28. Le, H. J., Liu, L. B., Chen, Y. D and Wan, W. X (2013). Statistical analysis of ionospheric responses to solar flares in solar cycle 23.Journal of Geophysical Research: Space Physics, 118(1): 576–582.
29. Liang, H., Yu, Y., Zhu, X., Wang, Y and Zhang, X (2023). Annual and semi-annual variations of electron density in the topside ionosphere observed by CSES.Frontiers in Earth Science, 11:1098483
30. Richmond, A. D. (1995). Ionospheric electrodynamics using magnetic apex coordinates. Journal of geomagnetism and geoelectricity, 47(2), 191-212
31. Price, C. (2016). ELF electromagnetic waves from lightning: The Schumann resonances. Atmosphere, 7(9), 116
32. Morozova, A. L., Barlyaeva, T. V and Barata, T (2020). Variations of TEC over the Iberian Peninsula associated with geomagnetic storms and solar UV flux during 2015, analyzed by Principal Component Analysis. Space Weather, 18: e2020SW002516.
33. Guerra, M., Cesaroni, C., Ravanelli, M and Spogli, L (2024). Traveling ionospheric disturbances detection: A statistical study of detrending

techniques, induced period error and near-real-time observables. Journal of Space Weather and Space Climate, 14:17
34. Hines, C. O (1960). Internal atmospheric gravity waves at ionospheric heights. Canadian Journal of Physics, 38(11):1441-1481.
35. Daubechies, I (1992). Ten lectures on wavelets. SIAM.
36. Mallat, S (2008). A wavelet tour of signal processing: The sparse way (3rd ed.). Academic Press
37. Harris, F. J (1978). On the use of windows for harmonic analysis with the discrete Fourier transform. Proceedings of the IEEE, 66(1):51-83.
38. Sentman, D. D (1995). Schumann resonance spectra in a two-scale-height Earth-ionosphere cavity. Journal of Geophysical Research: Space Physics, 101(A5): 9479-9487.
39. Takahashi, H., Figueiredo, C. A. O. B.,Essien, P., Wrasse, C. M., Barros, D., Nyassor, P. K., Paulino, I., Egito, F., Rosa, G. M and Sampaio, A. H. R (2022). Signature of gravity wave propagations from the troposphere to ionosphere. Annales Geophysicae, 40: 665–672.
40. Dowden, R. L., Brundell, J. B and Rodger, C. J. (2002). VLF lightning location by time of group arrival (TOGA) at multiple sites. Journal of Atmospheric and Solar-Terrestrial Physics, 64(7), 817-830.
41. Rodger, C. J., Werner, S., Brundell, J. B., Lay, E. H., Thomson, N. R., Holzworth, R. H and Dowden, R. L. (2009). Detection efficiency of the VLF World-Wide Lightning Location Network (WWLLN): Initial case study. Annales Geophysicae, 27: 2237-2248.
42. Laundal, K. M.,Ostgaard, N., Reistad, J. P., Tenfjord, P., Snekvik, K., Haaland, S. E and Milan, S. E (2010). Interhemispheric observations of emerging polar cap asymmetries. Journal of Geophysical Research: Space Physics, 115(A7): A07305.
43. Fechine, J., Wrasse, C. M., Takahashi, H., Mlynczak, M. G and Russell, J. M. (2008). Lower-mesospheric inversion layers over Brazilian equatorial region using TIMED/SABER temperature profiles. Advances in Space Research, 41(11):1447–1453
44. Rostoker, G (1979). The Auroral Electrojets. In: Akasofu, SI. (eds) Dynamics of the Magnetosphere. Astrophysics and Space Science Library, 78:201-11. Springer, Dordrecht.
45. Alexander, M. J and Barnet, C (2007). Using satellite observations to constrain parameterizations of gravity wave effects for global models. Journal of the Atmospheric Sciences, 64(5), 1652-1665.